

Modeling the Structure and Dynamics of Lithium Borosilicate Glasses with Ab Initio Molecular Dynamics Simulations

Takahiro Ohkubo,* Shingo Urata, Yutaka Immura, Taketoshi Taniguchi, Nanae Ishioka, Masamichi Tanida, Eiji Tsuchida, Lu Deng, and Jincheng Du



Cite This: *J. Phys. Chem. C* 2021, 125, 8080–8089



Read Online

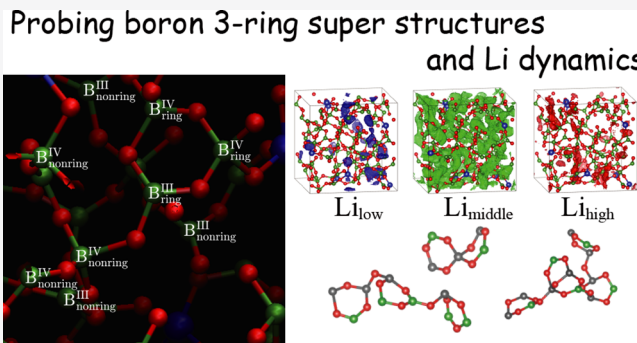
ACCESS |

Metrics & More

Article Recommendations

Supporting Information

ABSTRACT: Ion transport and the associated structures in glass materials are of interest in batteries and related materials. Herein, the atomic structures and dynamics of Li^+ in borosilicate glasses with high Li contents were studied using ab initio molecular dynamics (AIMD) simulations. The obtained bond distances and BO_4 fractions were in good agreement with the predictions of large-scale classical molecular dynamics (CMD) simulations with the latest potentials. The boron 3-ring super structures were successfully formed in the AIMD framework, overcoming a key limitation of CMD simulations. Consequently, the structures and Li^+ dynamics related to the boron 3-ring super structures were revealed by the AIMD simulations in this study. The dynamic properties of Li^+ and the glass network were investigated by Li^+ translation and vibration along with the libration of nonbridging O atoms. The Li^+ distributions for different Li mobilities were homogeneous in the glass network regardless of the nonbridging O species. The distributions were differentiated by the type of bonding cation (Si, three- and four-coordinated B atoms, and the boron 3-ring and nonring B atoms). The coupling motion between Li^+ and nonbridging O atoms is discussed based on the power spectra of Li^+ vibration and O libration. The results suggest that the decoupling of motion between network atoms and Li is key to developing glasses with higher ionic conductivity.



Classical molecular dynamics (CMD) simulations are a promising technique to simulate the structures of silicate and borosilicate glasses.^{18–20} Previous studies have mainly focused on glasses with low lithium contents [$x < 0.5$ in $x\text{Li}_2\text{O}-(1-x)\text{SiO}_2$].^{21–25} The lithium conduction mechanisms have been interpreted using the hopping model for Li sites in silicate glasses; Li mobility can be estimated based on mean-square displacement and the van Hove function of Li^+ calculated from MD trajectories.^{26,27} However, it is difficult to perfectly reproduce the atomic structure and macroscopic properties of boron-containing glasses using CMD simulations. Transferable empirical potentials have been developed to simulate a wide range of compositions for alkali borosilicate glasses.²⁸ These functions have been tuned to reproduce the fractions of four-coordinated B (B^{IV}) and the silicon Q_n (n is number of bridging oxygen atoms) structure observed by NMR and Raman spectroscopies. Although CMD simulations have

INTRODUCTION

Ionic conduction in oxide glasses is of broad interest for solid-state electrolytes in all-solid-state batteries.^{1–10} In addition, on the basis of the mobility of atoms in solid glasses, these glasses are widely used to manufacture porous glasses.^{11–14} Although ionic conduction ensures successful material production, the mechanism of ionic conduction in glass has remained unclear for decades. Mobile ions in glass are thought to move via hopping in voids formed within the complex glass network by host atoms (Si, B, and O), similar to vacancy in crystalline materials. In a simple interpretation of ionic conduction, the ions hop between voids around host atoms. In this interpretation, the ionic conduction is governed by the geometry of the void, which serves as a conduction path, and the extent of interaction with the host atoms. Thus, understanding these two factors is fundamental to providing insights into the mechanism of ionic conduction. The main difficulty in characterizing the conduction path is related to the complexity resulting from the random glass network. Crystalline materials with high ionic conductivity have clear ordering for a particular conduction path,^{15–17} providing a reasonable interpretation for high macroscopic conductivities. Measuring the complexity of the ionic conduction path remains a challenge in characterizing the glass structure.

Received: January 12, 2021

Revised: March 24, 2021

Published: April 9, 2021



achieved some success for borosilicate glasses, boron-related superstructures including 3-membered boron ring (i.e., the so-called “boron 3-ring super structures”) are not commonly observed in CMD simulations.^{29–31}

To obtain deep insights into the Li^+ conduction mechanism, one strategy is to separately define the conduction path and interaction between Li^+ and host atoms. The clarification of these mixed effects is helpful to design new high-performance glasses. Another barrier to understanding the nature of ionic conduction is the limitations of CMD. For borosilicate glasses, CMD simulations are generally performed with fixed charges and generalized force field parameters for targeted glasses. Atomic charges are assigned as fixed partial charges; for example, the atomic charge for oxygen is -1.2e in the CMD framework.^{19,28,32,33} This leads to Li^+ having a charge that is not $+1\text{e}$ to balance the total system charge. Enhancing the $\text{Li}-\text{Li}$ Coulombic interaction in Li-rich glasses may not guarantee the accurate simulation of Li^+ dynamics. In addition, the tendency of molecular orbitals to form boron-related superstructures cannot be accurately simulated by CMD, even if a polarizable force field is employed.^{34,35} Consequently, at the moment, the boron 3-ring super structures and the related Li^+ dynamics cannot be perfectly reproduced using CMD frameworks.

Although the simulation size and periods are limited to several hundreds atoms and pico seconds, the ab initio calculation can provide accurate glass model including electronic interactions based on the density functional theory (DFT). Ab initio molecular dynamics (AIMD) through glass melt to solidification have been less commonly employed, since the computational costs become very expensive compared to CMD. AIMD studies of sodium borosilicate and alumino borosilicate glasses have demonstrated the structural, dynamical, and vibrational properties can be reproduced with a good accuracy.^{36–38}

The main goal of this study was to understand Li conduction in Li_2O -rich borosilicate glasses from the perspective of the Li^+ diffusion path and dynamics. AIMD simulations were performed for three lithium borosilicate glasses with ~ 300 atoms over a relatively long time period (800 ps). In theory, AIMD can be used to simulate the boron-related superstructure and Li^+ interactions. However, a relatively fast quenching time and small simulation size are required to reduce the computational cost. The effects of these limitations were discussed by comparing the AIMD and CMD results by employing the recently developed borosilicate potentials.²⁸ Real glass samples with the same composition as the simulated glasses were also prepared to measure the conductivities and boron coordinates. To evaluate the fundamental characteristics of Li^+ conduction, we separately analyzed the glass structure related to Li^+ conduction and the interactions between Li^+ and host atoms.

■ GLASS SAMPLE

Three Li- and B-rich borosilicate glasses were prepared by conventional melt-quenching methods. The glass compositions were 40 Li_2O –30 B_2O_3 –30 SiO_2 (40L30B30S), 40 Li_2O –50 B_2O_3 –10 SiO_2 (40L50B10S), and 60 Li_2O –25 B_2O_3 –15 SiO_2 (60L25B15S). Stoichiometric raw materials (Li_2CO_3 , SiO_2 , and B_2O_3) for the three compositions were mixed and melted within a platinum crucible in an electronic furnace at 1273.15 K. The glass melts were rapidly cooled using a rollout machine to prepare flake-shaped glasses (hereinafter referred to as glass

flakes). The obtained glasses were transparent and contained no crystalline phases. The actual compositions were verified by inductively coupled plasma-atomic emission spectroscopy (ICP-AES), which showed that the difference between the nominal and actual compositions was less than 3% by mass. The glass densities were measured by gas pycnometry. The ionic conductivities were estimated using glass flakes with diameters of 10 mm and thicknesses of 0.3 mm. Gold electrodes (diameter = 4 mm) were formed via vapor deposition on both surfaces of the glass flake. AC impedance measurements were performed using an impedance analyzer (Solartron SI 1287) at room temperature. The frequency range for the measurements was varied from 0.1 Hz to 10 MHz. The compositions, densities, and conductivities are summarized in Table 1. The conductivity of 40L30B30S was unmeasurable due to high resistance, indicating a low conductivity less than 5×10^{-9} S/cm.

Table 1. Glass Composition, Density, and Ionic Conductivity^a

sample	Li_2O (mol %)	B_2O_3 (mol %)	SiO_2 (mol %)	density (g/cm ³)	conductivity (S/cm)
40L30B30S	40	30	30	2.31	$<10^{-9}$
40L50B10S	40	50	10	2.30	2.8×10^{-7}
60L25B15S	60	25	15	2.20	8.7×10^{-7}

^aThe conductivity of 40L30B30S could not be measured due to its low value ($< 5 \times 10^{-9}$ S/cm).

The atomic structure of boron in the samples was investigated by ¹¹B magic-angle spinning nuclear magnetic resonance (MAS NMR) spectroscopy. ¹¹B MAS NMR experiments were conducted using a JEOL-600 instrument under a 14.10-T magnetic field at 192.559 MHz. All spectra were obtained after a single pulse with a width of 0.1 μs , corresponding to a flip angle of $\pi/6$ with a recycling time of 15 s. The chemical shifts were referenced to 1.0 M H_3BO_3 at 19.6 ppm. The ¹¹B quadrupolar line shapes in the NMR spectra were deconvoluted to identify B species using a homemade program incorporating mrsimulator.³⁹

■ COMPUTATIONAL METHODS

AIMD simulations were carried out for three borosilicate glasses with the same compositions as the experimental samples. All simulations were performed using FEMTECK,^{40–42} our own simulation code that enables faster simulation of amorphous materials. The code uses adaptive finite-element methods for polynomial basis functions in real space instead of ordinary plane-wave functions in periodic systems. As a result, simulations of glass melting and solidification are possible within the AIMD framework. All production runs were performed with an average cutoff energy of 75–85 Ry. Norm-conserving pseudopotentials were used to represent the ionic cores.^{43,44} The MD time step was 2.0 fs, and the wave functions were smoothly extrapolated from the previous time steps. Other details of FEMTECK are found in “Summary of FEMTECK” of Supporting Information.

The initial glass structures were built with random atomic positions to satisfy the compositions in the cell corresponding to the experimental density. The total numbers of atoms were 288, 320, and 280 for 40L30B30S, 40L50B10S, and 60L25B15S, respectively. First, CMD using a Buckingham-type function²⁰ was carried out at 3,000 K under the NVT

ensemble. After equilibration in the CMD framework, the simulation was switched to AIMD. Complete annealing to lose the CMD structure was carried out for 100 ps at 3000 K. Subsequently, the glass melt was cooled to 1600 K and equilibrated for 200 ps. At this stage, all atoms diffused freely in the cell, indicating that the system was completely melted. Indeed, all network forming atoms (Si, B, and O) reached diffusive regime (see MSD plots in Figure S1) beyond 20 ps at this temperature. And the systems were equilibrated for 200 ps and the diffusion distances of each species were larger than half of the simulation cell size to ensure equilibration of the melt.

Next, the glass melt was cooled to 800 K at a moderate cooling rate of 8 K/ps to reproduce the glass structure.^{33,45} After equilibration at 800 K, the atomic trajectories were recorded for a minimum of 400 ps.

As a comparison, CMD simulations using the same number of atoms (~300) as the AIMD simulations and a larger (~7000) number of atoms were performed for the three systems to check the validity of the simulation size in AIMD. The LAMMPS package was employed for the CMD simulations.⁴⁶ Recently, developed force field parameters corresponding to the glass composition were used in the CMD simulations.²⁸ These parameters can reproduce the fraction of four-coordinated B (B^{IV}) in alkali borosilicate glasses as well as the recently developed shell model.⁴⁷ Details regarding the CMD procedure and glass composition can be found in the Supporting Information section Comparison with Classical Molecular Dynamics and Table S1.

RESULTS AND DISCUSSION

Glass Structure. The ^{11}B MAS NMR spectra with deconvoluted lines for 40L30B30S, 40L50B10S, and 60L25B15 are shown in Figure 1. Deconvolution was conducted based on three peaks corresponding to a four-coordinated B atom (B^{IV}) and two three-coordinated rings and nonring B atoms (B_{ring}^{III} and B_{nonring}^{III}). The line shape of B^{IV} was fit by a pseudo-Voigt function to obtain the symmetric line shape for a small quadrupolar coupling constant (<1 MHz) resulting from tetrahedral structure with higher three-dimensional symmetry.⁴⁸ The spinning sidebands marked with “*” on the whole spectra are shown in insets of Figure 1. The intensities of B^{IV} on sidebands were relatively higher than the main spectra. These observations reflect residual interactions (first-order quadrupolar, dipolar, and chemical shift anisotropy interactions) under MAS. Main contribution is first-order quadrupolar interaction. The strong intensity of sidebands for B^{III} is the reason for higher first-order quadrupolar compared to B^{IV} . These residual interactions were also weakened with atomic motion, suggesting that B_{ring}^{III} and B_{nonring}^{III} have higher degree of atomic motion compared to B^{IV} . Two species models (B^{IV} bridging to one or two SiO_4) for alkali borosilicate glasses were used to make a fitting model.^{49,50} However, the three spectra in this study were well fit by a one-peak model due to line broadening resulting from the structural distribution. A quadrupolar line shape was simulated for B_{ring}^{III} and B_{nonring}^{III} . The isotropic chemical shift (δ_{iso}) and quadrupolar coupling constant (C_Q) were adjustable parameters, while the Gaussian broadening factor B_F and quadrupolar asymmetry parameter (η) were fixed at 0.2 and 500 Hz, respectively, following previous ^{11}B NMR studies on alkali borosilicates.^{49,50} The experimental spectra were well reproduced by the simulations; however, the uncertainty of the fitting model with fixed values of η and B_F is discussed here. We tested the validity of the

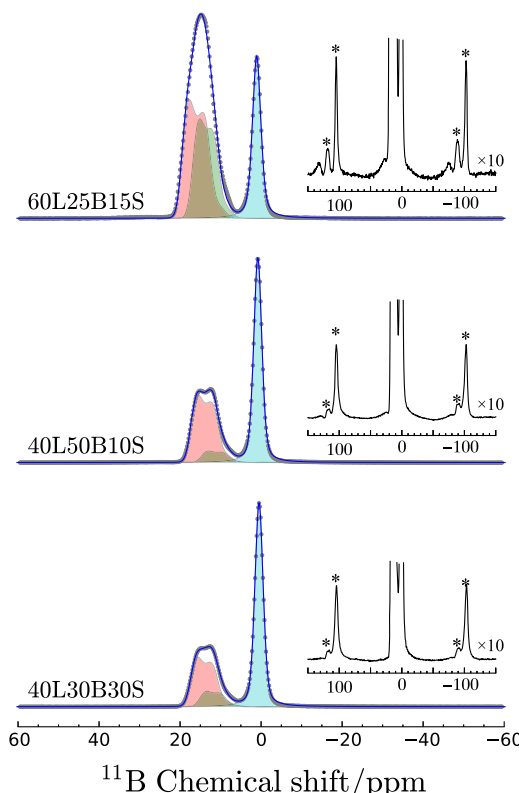


Figure 1. ^{11}B MAS NMR spectra (gray dots) and deconvoluted lines (solid colors) for 40L30B30S, 40L50B10S, and 60L25B15. Gray points and blue solid lines are the experimental and simulated data, respectively. Solid red, green, and blue colors are assigned to B_{ring}^{III} , B_{nonring}^{III} , and B^{IV} , respectively. The chemical shift and quadrupolar coupling constant were determined by fitting. The Gaussian broadening and quadrupolar asymmetry parameter were respectively fixed to 500 Hz and 0.2 for B_{ring}^{III} and B_{nonring}^{III} . The whole spectra including spinning sidebands with 10 times intensity were shown in insets. The sidebands were marked with an asterisk (*).

fitting model with variable η and B_F . The resulting parameters and simulated results are shown in Figure S2 and Table S8. The differences in the atomic fractions between the fitting models were within 5%, indicating that the atomic fractions derived from the experimental spectra are accurate. The experimental fractions are summarized in Table 2, which includes results from the AIMD-derived structure and the B^{IV} fraction expected from the Dell–Bray–Xiao (DBX) model modified by Du and Stebbins.^{51–53} The atomic fractions calculated from the AIMD-derived structure were determined from the coordination number using a cutoff distance of 2.0 Å for the B–O pair correlation function (Figure S4).

The experimental B^{IV} atomic fractions for the three systems were ~18% higher than those determined from the DBX model and the AIMD-derived structures. The projections of the DBX model were in good agreement with the AIMD-derived atomic fractions (within 4%). The observed deviation might be explained by the system size or the quenching rate of the simulation.⁵⁴ The effect of system size was evaluated by comparing the CMD simulations of the same size as the AIMD simulations (CMD300) with the 7000-atom CMD (CMD7000) systems for the three glasses (described in Supporting Information). All atomic fractions of B^{IV} and other species are given in Tables S2–S4. The B^{IV} fractions obtained from both CMD simulations were consistent with the AIMD

Table 2. Atomic Fractions (%) Obtained from Experimental ^{11}B MAS NMR Spectra^a

	NMR			AIMD			DBX	
	$\text{B}_{\text{ring}}^{\text{III}}$	$\text{B}_{\text{nonring}}^{\text{III}}$	B^{IV}	$\text{B}_{\text{ring}}^{\text{III}}$	$\text{B}_{\text{nonring}}^{\text{III}}$	B^{IV}	$\text{B}_{\text{ring}}^{\text{III}} + \text{B}_{\text{nonring}}^{\text{III}}$	B^{IV}
40L30B30S	32.7	9.8	57.5	10.4	50.2	39.3	58.3	41.7
40L50B10S	40.9	6.8	52.2	17.4	42.6	40.0	56.6	43.4
60L25B15S	41.8	32.7	25.5	3.3	87.8	8.9	94.5	5.5
	CMD0300			CMD7000				
	$\text{B}_{\text{ring}}^{\text{III}}$	$\text{B}_{\text{nonring}}^{\text{III}}$	B^{IV}	$\text{B}_{\text{ring}}^{\text{III}}$	$\text{B}_{\text{nonring}}^{\text{III}}$	B^{IV}		
40L30B30S	0.1<	66.6	33.4	0.1<	64.5	35.4		
40L50B10S	0.2	54.2	45.6	0.1	53.5	46.4		
60L25B15S	0.1<	92.1	7.9	0.1<	91.5	8.5		

^aThe atomic fractions calculated from the AIMD-derived structure and expected from the DBX model are also shown.

and DBX predictions. Consequently, the deviation resulting from simulation size was within the statistical error. These results indicate that system size is not a central reason for the discrepancy between the experimental and AIMD simulation results. Thus, the rapid quenching rate, which cannot be avoided in CMD simulations, may be a major reason for the deviation. The other possible reasons to explain the discrepancy are the system size and experimental uncertainties originated from fitting model with a single set of C_Q and η for $\text{B}_{\text{ring}}^{\text{III}}$ and $\text{B}_{\text{nonring}}^{\text{III}}$. Quadrupole features of B^{III} on the spectra measured at 14.10-T may be diminished on the peaks. In addition, broad distributions of C_Q and η cause large uncertainties to quantify these fractions. We concluded that although the deviation of the AIMD B^{IV} atomic fraction from the experimental value was non-negligible, the AIMD-derived structure can at least provide a reliable glass structure in theory.

The Si/B mixing of bridging oxygen (O^{II}) is calculated from fractions of $\text{Si}-\text{O}^{\text{II}}-\text{Si}$, $\text{Si}-\text{O}^{\text{II}}-\text{B}$, and $\text{B}-\text{O}^{\text{II}}-\text{Si}$ bonds (Tables S2–S4). These fractions follow the glass compositions, meaning that the glass networks are composed of ideal Si/B mixing without B and Si-rich phase separation. Charge compensators for Li^+ are assigned to negatively charged atoms (nonbridging oxygen (O^{I}) and B^{IV}). Numbers of Li^+ were balanced to total numbers of O^{I} and B^{IV} for the AIMD-derived structures. The populations of B^{IV} as the charge compensator are 8.51%, 25.91%, and 2.11% for 40L30B30S, 40L50B10S, and 60L25B15S, respectively.

Three- and four-coordinated B units were classified into three-membered boron ring ($\text{B}_{\text{ring}}^{\text{III}}$ and $\text{B}_{\text{ring}}^{\text{IV}}$) in the super structures and nonring ($\text{B}_{\text{nonring}}^{\text{III}}$ and $\text{B}_{\text{nonring}}^{\text{IV}}$) units, as shown in left image of Figure 2. The extracted boron 3-ring super structures were drawn in the right image of Figure 2. A clear difference between AIMD and CMD was found in the formation of boroxol rings, as shown in Table 2. The generation of the boron 3-ring super structures was only rarely observed in the CMD framework, despite the large simulation size. The inability of CMD to reproduce superstructural groups of boron is a well-known limitation of this method.^{31,55} Although AIMD simulation can reproduce the boron 3-ring super structures, it underestimates the fraction of $\text{B}_{\text{ring}}^{\text{III}}$ compared to the experimental results.

A possible explanation for the discrepancy between the AIMD results and experimental observation may be the rapid quenching rate in the simulation compared to the experiments. It is worth noting that the simulation of glass is restricted by the quenching rate, even if the simulation is conducted in the AIMD framework at the slowest possible quenching rate.

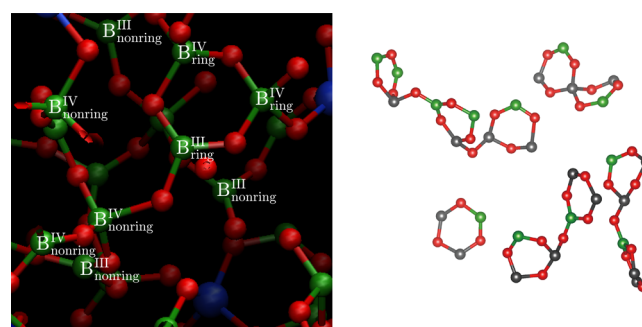


Figure 2. Assigned B units of 40L50B10S are shown in the left image (green, B; red, O; blue, Si). The right image is visualization of the boron 3-ring super structures (other atoms not shown). $\text{B}_{\text{ring}}^{\text{III}}$ and $\text{B}_{\text{ring}}^{\text{IV}}$ are drawn with green and gray balls.

However, since the AIMD method reproduced a realistic ring structure, we can at least discuss the structure and Li^+ dynamics related to the boron 3-ring super structures.

The bond lengths obtained from AIMD and CMD simulations are summarized in Tables S5–S7. These data are classified by specific atomic units; for example, the lengths of $\text{B}_{\text{ring}}^{\text{III}}-\text{O}$ and $\text{B}_{\text{ring}}^{\text{IV}}-\text{O}$, where $\text{B}_{\text{ring}}^{\text{III}}$ and $\text{B}_{\text{ring}}^{\text{IV}}$ are B atoms in the boron 3-ring super structures, were estimated separately. O^{II} was also classified as $\text{O}_{\text{ring}}^{\text{II}}$ in the boron 3-ring super structures. The average $\text{B}_{\text{ring}}^{\text{III}}-\text{O}_{\text{ring}}^{\text{II}}$ and $\text{B}_{\text{ring}}^{\text{IV}}-\text{O}_{\text{ring}}^{\text{II}}$ bond lengths in crystalline dilithium oxide tris(diborate) are 1.3725 (1.34, 1.41, 1.39, and 1.35 Å) and 1.475 Å (1.45 and 1.50 Å), respectively. The AIMD results gave $\text{B}_{\text{ring}}^{\text{III}}-\text{O}_{\text{ring}}^{\text{II}}$ bond lengths of 1.392, 1.395, and 1.415 Å for 40L30B30S, 40L50B10S, and 60L25B15S, respectively. Longer distances of 1.494, 1.502, and 1.536 Å were obtained for $\text{B}_{\text{ring}}^{\text{IV}}-\text{O}_{\text{ring}}^{\text{II}}$ in 40L30B30S, 40L50B10S, and 60L25B15S, respectively. These bond lengths are in good agreement with the crystalline structures, suggesting that the boron 3-ring super structures in crystalline glasses are effectively maintained in the borosilicate glasses.

The AIMD bond lengths are also in agreement with the results of geometrical optimization by density functional theory for the CMD-derived structure.⁴⁷ It is worth noting that the bond lengths derived from CMD simulations using proposed potentials were well reproduced by AIMD; however, large discrepancies were observed in the ring-related bond lengths (e.g., $\text{B}_{\text{ring}}^{\text{IV}}-\text{O}_{\text{ring}}^{\text{II}}$). This difference may be related to the insufficient structural stability to form the boron 3-ring super structures in CMD. The use of AIMD allowed the detailed investigation of the structural properties of the boron 3-ring super structures in this study. The visual representation of the

boron 3-ring super structures shown in Figure S3 of Supporting Information indicates the coexistence of $B_{\text{ring}}^{\text{III}}$ and $B_{\text{ring}}^{\text{IV}}$ in the boron 3-ring super structures with approximately the same atomic fractions. This provides the first evidence of the ring structure in alkali borosilicate glasses. The bond angle distributions (BADs) of O–B–O and B–O–B in the boron 3-ring super structures were individually estimated for $B_{\text{ring}}^{\text{III}}$ and $B_{\text{ring}}^{\text{IV}}$ (Figure 3). All BADs were normalized by area, and the

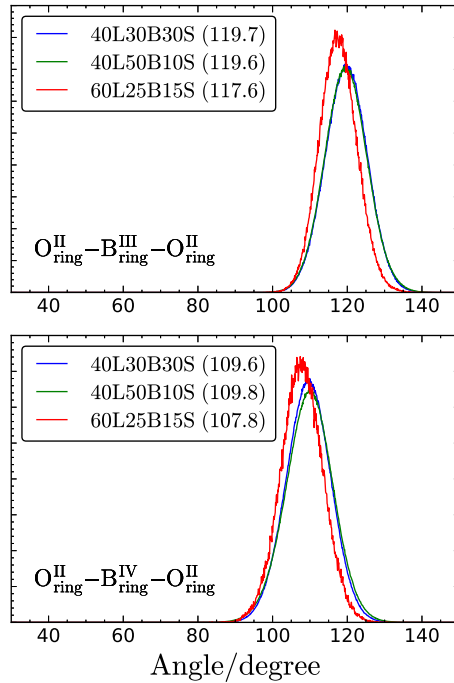


Figure 3. Bond angle distributions of O–B–O in the boron 3-ring super structures for 40L30B30S, 40L50B10S, and 60L25B15S. The decomposed distributions of $O_{\text{ring}}^{\text{II}}\text{--}B_{\text{ring}}^{\text{III}}\text{--}O_{\text{ring}}^{\text{II}}$ and $O_{\text{ring}}^{\text{II}}\text{--}B_{\text{ring}}^{\text{IV}}\text{--}O_{\text{ring}}^{\text{II}}$ were estimated separately, and all distributions were normalized by area. The average angles are given in parentheses within the legend.

average angles are shown in the legends of each figure. The BADs in the boron 3-ring super structures of 40L30B30S and 40L50B10S were nearly the same, whereas that for 60L25B15S was shifted to a lower angle. These values are in good agreement with the angles of perfect triangular (120°) and tetrahedral (109.47°) units. In the boron 3-ring super structures of the crystalline compound dilithium oxide tris(diborate), $\text{Li}_2\text{O}(\text{B}_2\text{O}_3)_3$, the $O_{\text{ring}}^{\text{II}}\text{--}B_{\text{ring}}^{\text{III}}\text{--}O_{\text{ring}}^{\text{II}}$ and $O_{\text{ring}}^{\text{II}}\text{--}B_{\text{ring}}^{\text{IV}}\text{--}O_{\text{ring}}^{\text{II}}$ bond angles are 121° and 112° , respectively.³⁶ The angles in the crystalline structure are larger than those in the glass, suggesting that the glass structure without periodic alignment is more relaxed. As a result, the BADs are closer to the ideal structure in which $O_{\text{ring}}^{\text{II}}\text{--}B_{\text{ring}}^{\text{III}}\text{--}O_{\text{ring}}^{\text{II}}$ and $O_{\text{ring}}^{\text{II}}\text{--}B_{\text{ring}}^{\text{IV}}\text{--}O_{\text{ring}}^{\text{II}}$ are sp^2 and sp^3 hybridized, respectively. A shift toward lower angle was also found for 60L25B15S. Because the glass network in 60L25B15S is broken at high Li contents, as shown in Figure S3, the boron 3-ring super structures is not a member of the glass network. Consequently, the isolated ring terminated with O^{I} is distorted under strong interaction with Li^+ .

The nature of the Li^+ conduction path was investigated based on the O–Li pair correlation functions for different O species, which can highlight the preferential path for Li^+ conduction. Li^+ translation is thought to be caused by

migration between stable sites around O. An important analysis is to determine specific sites for Li^+ conduction. O^{I} and O^{II} were identified using a cutoff distance of 2.3 \AA based on the Si–O and B–O pair correlation functions (Figure S4). The $\text{O}^{\text{I}}\text{--Li}$ and $\text{O}^{\text{II}}\text{--Li}$ pair correlation functions are shown in Figure 4. The running coordination number (RCN) is also

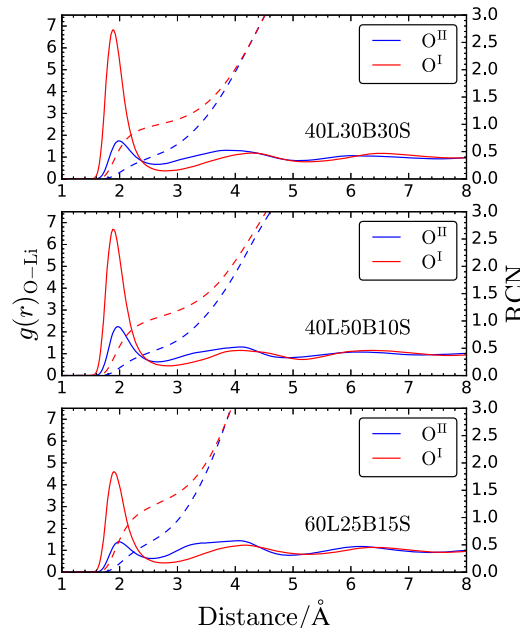


Figure 4. O–Li pair correlation functions for 40L30B30S, 40L50B10S, and 60L25B15S. The functions were calculated for bridging and nonbridging O atoms. The RCNs of Li around O are shown by the dotted lines on the right axis.

displayed in Figure 4. These functions can be used to inspect the preferential coordination structure of Li with O^{I} or O^{II} . The Li coordination numbers for O^{I} and O^{II} at 2.6 \AA were approximately 1.2 and 0.5, respectively, for the three systems. Therefore, the preferential sites for Li^+ were the first coordination shell around O^{I} regardless of the composition. The first peak position of O^{I} was slightly shorter than that of O^{II} , meaning that the interaction with Li is stronger for O^{I} . These differences in Li coordination structure between O^{I} and O^{II} are thought to reflect the Coulombic interaction resulting from the electronic structures of O^{I} and O^{II} . The localized electron on O^{I} derived from AIMD preferentially attracts Li^+ compared to O^{II} , leading to a shorter O–Li distance and higher coordination number.

Dynamics. To explain Li^+ conductivity more directly, the dynamic properties were investigated by translational and vibrational analyses. The MSD was calculated from the position and number of Li^+ (r and N , respectively) to estimate the self-diffusion coefficient D :

$$\text{MSD}(t) = \frac{1}{N} \sum_{i=1}^N |\mathbf{r}_i(t_0) - \mathbf{r}_i(t_0 + t)|^2 \quad (1)$$

$$D = \frac{1}{6} \lim_{t \rightarrow \infty} \frac{d}{dt} \text{MSD}(t) \quad (2)$$

The MSDs were obtained from 200 ps trajectories with different starting time points, as shown in Figure 5. Different stages with different dynamics were previously found in lithium

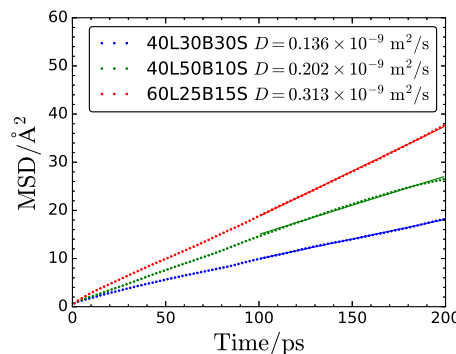


Figure 5. Mean square displacements of Li in 40L30B30S, 40L50B10S, and 60L25B15S at 800 K. The solid lines show the fitting results of linear regression.

silicate glasses and were attributed to the heterogeneous dynamics of Li^+ .^{23,26,27} The short time regime of the MSD reflects the cage-like limitation of the translational motion of Li^+ in the voids. When each ion moves freely in space, the distribution of the translational distance takes the form of a Gaussian function. In this regime, a linear relationship is found between time and MSD, and the slope of the line gives the self-diffusion coefficient for long translational motion. Three clear lines were obtained for 40L30B30S, 40L50B10S, and 60L25B15S after 100 ps; consequently, the Li^+ self-diffusion coefficients were calculated via regression for the last 100 ps to be 0.136, 0.202, and $0.313 \times 10^{-9} \text{ m}^2/\text{s}$, respectively, on the order of the experimental Li^+ conductivity. The time scale of molecular dynamics does not allow the estimation of low diffusion coefficients at room temperature. Although resistance from sample–electrode interface might affect the experimental conductivity for the glass flakes, the resistance was neglected in the simulation under periodic conditions. However, the orders of the Li^+ self-diffusion coefficients derived from AIMD at 800 K are reasonable. It should be noted that the host atoms (Si, B, and O) show only vibrational motion around the center of mass.

The distribution of Li^+ translation for 200 ps was calculated from trajectories with different starting time points (Figure 6). This distribution corresponds to the self-part of the van Hove function for Li^+ . The distribution for 60L25B15S exhibits a Gaussian-like shape, while higher frequencies over a shorter distance (within 2 Å) are found for 40L30B30S and 40L50B10S. In Figure 6, three types of Li^+ are labeled and colored to differentiate Li^+ mobility. The thresholds differentiating the longer and shorter distances were set to 2 and 9 Å, respectively. High, middle, and low Li^+ mobility are labeled as Li_{low} , $\text{Li}_{\text{middle}}$, and Li_{high} and indicated by blue, green, and red bars in Figure 6, respectively. Although these distinctions are arbitrary, these species are good indicators to discuss the specific structures around Li^+ based on differences in mobility. A low content of Li_{low} was found for 60L25B15S, indicating that more Li^+ can contribute to ionic conduction in 60L25B15S than in 40L30B30S and 40L50B10S. This explains the higher conductivity of 60L25B15S compared to 40L30B30S and 40L50B10S. The contents of Li_{high} are similar in 40L50B10S and 60L25B15S (6.2% and 5.2%, respectively), suggesting that the higher conductivity results from the vanishing Li_{low} in 40L50B10S. The absence of low-mobility Li^+ may create hopping sites for Li^+ conduction in the glass network.

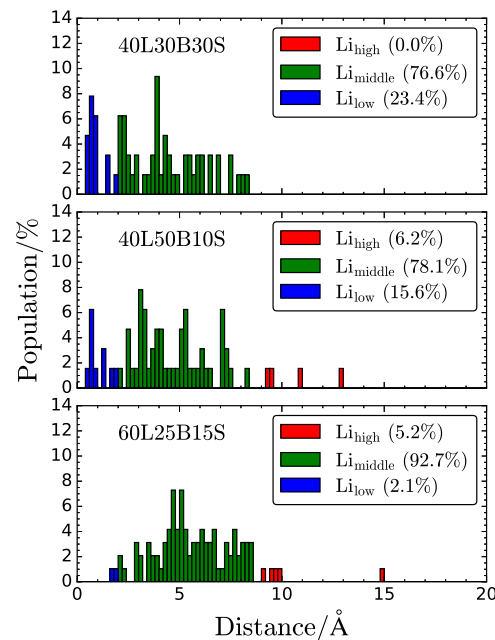


Figure 6. Histograms of Li^+ translation over 200 ps trajectories for 40L30B30S, 40L50B10S, and 60L25B15S at 800 K. The bars are colored based on thresholds of 2 and 9 Å to differentiate Li^+ with high (red; Li_{high}), middle (green; $\text{Li}_{\text{middle}}$), and low (blue; Li_{low}) mobility. The fractions of Li_{high} , $\text{Li}_{\text{middle}}$, and Li_{low} are displayed on each panel.

The Li^+ diffusion space in the simulation cell was investigated by counting number of visits to a voxcel, which is small space partitioned with a $100 \times 100 \times 100$ regular grid in three-dimensional space. The Li^+ diffusion space in the simulation cell was drawn by iso-surface rendering for the voxels above 20 visits for 400 ps. Figure 7 displayed the colored iso-surface rendering for all Li, Li_{low} , $\text{Li}_{\text{middle}}$, and Li_{high} differentiated based on mobility in Figure 6. Si, B, and O were also displayed colored balls at the average position for 400 ps. The simulation cell of 60L25B15S was almost filled with Li^+ diffusion space compared to those of 40L30B30S and 40L50B10S, which is consistent with the orders of the Li^+ self-diffusion coefficients. The Li^+ diffusion space of 40L30B30S is tortuous, and a part of space is blank. It seems that a part of cavity space is blocked with the glass network. Ordered diffusion path for all Li^+ species is not confirmed from all images, meaning that the random diffusion path is the nature of the borosilicate glasses in this study.

The effective Li^+ diffusion paths were locally evaluated based on the O^{I} and B^{IV} partial correlation functions with Li_{low} , $\text{Li}_{\text{middle}}$, and Li_{high} . The O^{I} and B^{IV} are assigned to charge compensator for Li^+ . Li^+ is also preferentially coordinated to O^{I} , as shown in Figure 4. Furthermore, we differentiated O^{I} species to capture the Li^+ conduction path based on the bonding cation species (B^{III} , B^{IV} , and Si). The O^{II} partial correlation functions were also calculated for Li_{low} , $\text{Li}_{\text{middle}}$, and Li_{high} . The 15 pair correlation functions for these combinations are shown in Figure S5 of Supporting Information. The coordination numbers with Li_{high} , $\text{Li}_{\text{middle}}$, and Li_{low} were calculated using the cutoff distance of 2.80, 3.60, and 2.55 Å for O^{I} , B^{IV} , and O^{II} , which corresponds to the first minimums. These coordination numbers can be used to probe the Li^+ diffusion paths surrounding a particular O^{I} species. In order to estimate preferential coordination, the coordination numbers of the O^{I} , B^{IV} , and O^{II} species are rescaled by number of Li_{high} .

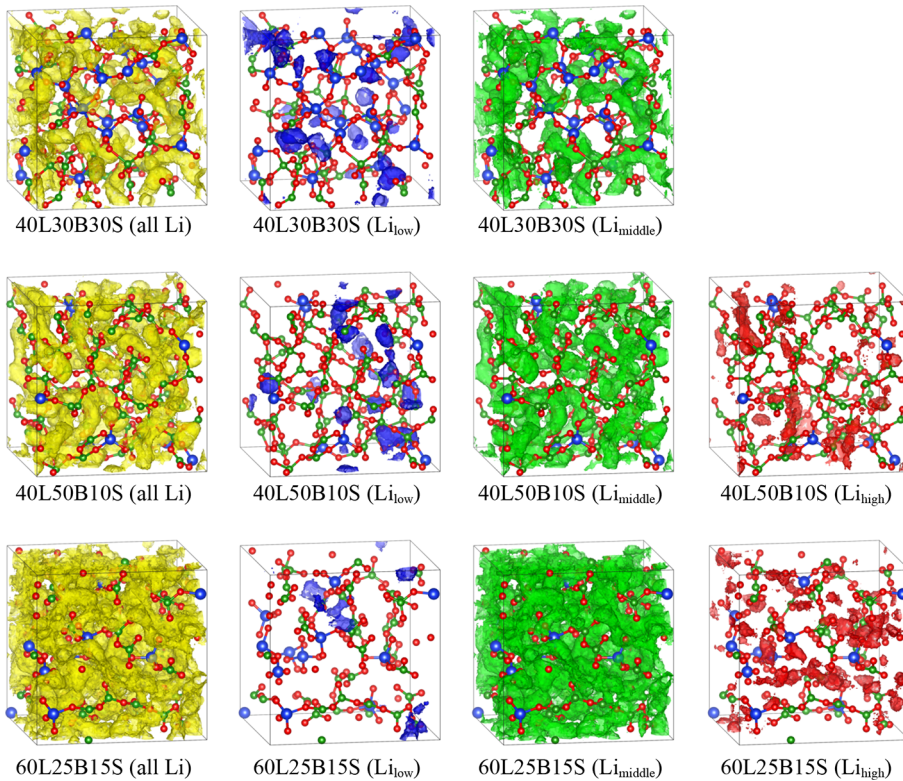


Figure 7. Iso-surface drawing for Li^+ diffusion over 400 ps trajectories for 40L30B30S, 40L50B10S, and 60L25B15S at 800 K. Yellow, blue, green, and red volumes correspond to those of all Li, Li_{low} , $\text{Li}_{\text{middle}}$, and Li_{high} differentiated by displacements as shown in Figure 6. Blue, green, and red balls are Si, B, and O. These balls are drawn at the average positions over 400 ps.

$\text{Li}_{\text{middle}}$, and Li_{low} and summarized in Table 3. These values are time-average results for all simulation runs. The cation species

Table 3. Coordination Numbers Based on Pair Correlation Functions (Figure S5) for a Cutoff Distance^a

	40L30B30S	40L50B10S	60L25B15S
$\text{O}^{\text{I}}(\text{B}^{\text{III}})-\text{Li}_{\text{low}}$	0.049	0.045	0.052
$\text{O}^{\text{I}}(\text{B}^{\text{IV}})-\text{Li}_{\text{low}}$	0.029	0.004	0.040
$\text{O}^{\text{I}}(\text{Si})-\text{Li}_{\text{low}}$	0.047	0.071	0.017
$\text{B}^{\text{IV}}-\text{Li}_{\text{low}}$	0.082	0.078	0.022
$\text{O}^{\text{II}}-\text{Li}_{\text{low}}$	0.020	0.022	0.016
$\text{O}^{\text{I}}(\text{B}^{\text{III}})-\text{Li}_{\text{middle}}$	0.049	0.054	0.042
$\text{O}^{\text{I}}(\text{B}^{\text{IV}})-\text{Li}_{\text{middle}}$	0.061	0.009	0.034
$\text{O}^{\text{I}}(\text{Si})-\text{Li}_{\text{middle}}$	0.047	0.043	0.041
$\text{B}^{\text{IV}}-\text{Li}_{\text{middle}}$	0.074	0.073	0.077
$\text{O}^{\text{II}}-\text{Li}_{\text{middle}}$	0.018	0.020	0.018
$\text{O}^{\text{I}}(\text{B}^{\text{III}})-\text{Li}_{\text{high}}$		0.047	0.038
$\text{O}^{\text{I}}(\text{B}^{\text{IV}})-\text{Li}_{\text{high}}$		0.010	0.015
$\text{O}^{\text{I}}(\text{Si})-\text{Li}_{\text{high}}$		0.051	0.049
$\text{B}^{\text{IV}}-\text{Li}_{\text{high}}$		0.079	0.047
$\text{O}^{\text{II}}-\text{Li}_{\text{high}}$		0.021	0.018

^a O^{I} was differentiated based on the bonding cation species (B^{III} , B^{IV} , and Si). Li^+ was also classified into three species with different displacements over 200 ps, as shown in Figure 6.

in parentheses for each O^{I} indicates the bonding cation. Number of Li^+ around O^{II} is less than those of B^{IV} and O^{I} regardless of Li^+ mobility and the glass composition. Small O^{I} (B^{IV}) coordination numbers were found for Li_{low} and $\text{Li}_{\text{middle}}$ in 40L50B10S, indicating that the space around O^{I} (B^{IV}) contains less Li^+ concentration. This trend was not observed in

40L30B30S and 60L25B15S. The arrangement of the boron 3-ring super structures shown in Figure S3 may contribute to the low O^{I} (B^{IV}) coordination number. Although the coordination number of O^{I} (B^{IV}) in 40L50B10S is characteristically low, no clear dependence of coordination number on B^{IV} and O^{I} species was found in the three glasses. This suggests that the Li^+ conduction path surrounding a particular O^{I} species is not recognized. Li^+ is randomly distributed in the space formed with natural glass networks, and diffusion occurs homogeneously in the space around B^{IV} and all O^{I} species.

The Li^+ diffusion is correlated not only to geometry of the diffusion space but also dynamics of atoms surrounding the diffusion space. The Li^+ translation is associated with a coupling motion between Li^+ and O^{I} to which highly mobile Li^+ preferably interacts. The relationship between the coupling motion and Li^+ translation is not fully understood.⁵⁷ The rotation/reorientation of anions may contribute to propel passage of the cation from sites to sites. On the other hand, complete coupling motion might be also observed for stationary vibrational motion between Li^+ and O^{I} without passage.

The coupling motions of O^{I} libration and Li^+ vibration were directly estimated from the power spectra, $F(\nu)$, obtained from the Fourier transform of the normalized correlation function:⁵⁸

$$F(\nu) = \int_0^\infty \frac{\langle \nu(0) \cdot \nu(t) \rangle}{\langle \nu(0)^2 \rangle} \exp(-i2\pi\nu t) dt \quad (3)$$

where $\nu(t)$ is either the Li^+ velocity or O^{I} angular velocity. The O^{I} angular velocity was calculated from the O^{I} velocity and vectors between O^{I} and bonding cation (Si and B) coordinates. The power spectra of Li^+ vibration and O^{I} libration are shown

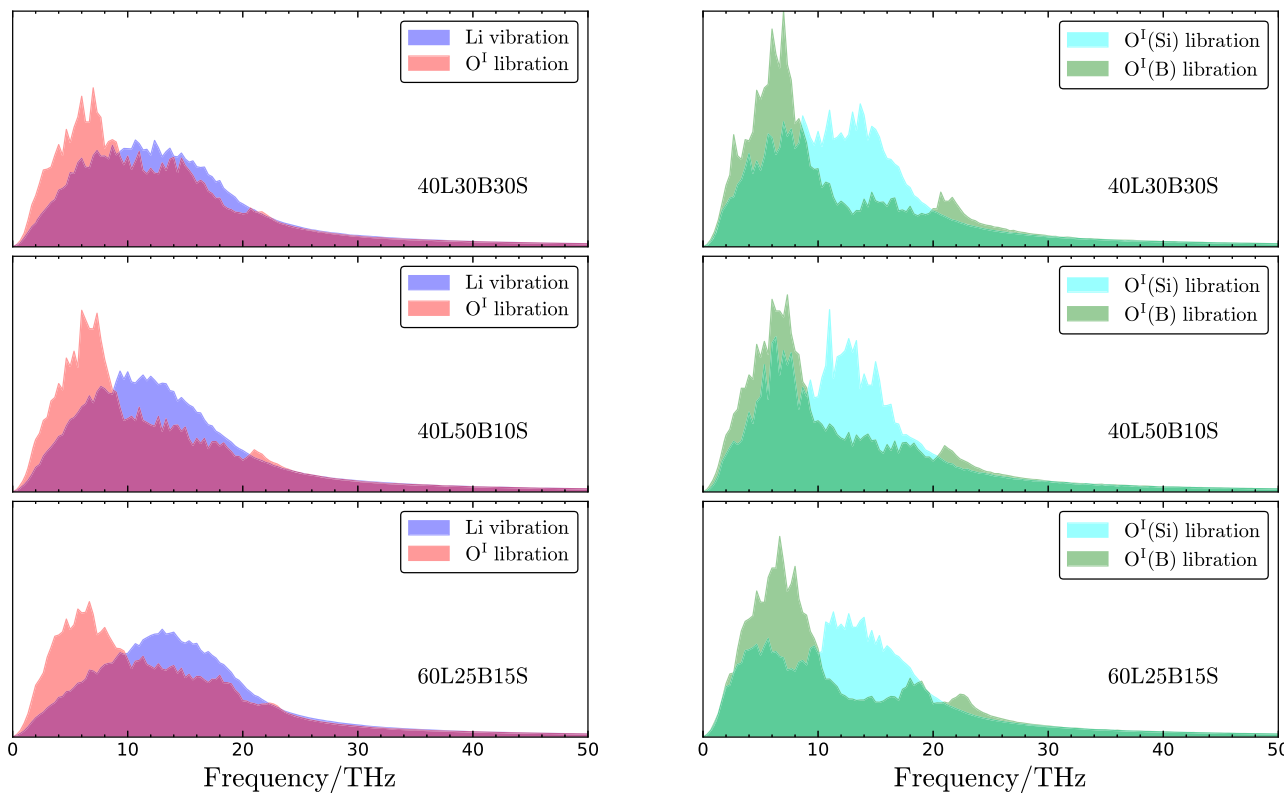


Figure 8. Power spectra of Li^+ vibrational and O^1 librational motions were shown in the left figure. Partial libration spectra of O^1 bonding to Si and B were also indicated in the right figure. These spectra were calculated from the autocorrelation functions of Li^+ velocity and O^1 angular velocity.

in Figure 8. Furthermore, partial libration spectra of O^1 were individually calculated for O^1 bonded to Si and B. The similarity of these spectra allows us to estimate the coupling motion. Peaks at around 5.0 THz are found in the O^1 libration spectra of the three glasses, while the peaks in the Li^+ vibrational spectra are dependent on the composition. The best overlap is observed for 40L30B30S, indicating that the Li^+ vibrational and O^1 librational motions are well coupled in this composition. The peaks ranging from 10 to 18 THz were assigned to O^1 bonding to Si as shown in the partial libration spectra. The peak in the Li^+ vibrational spectrum for 60L25B15 is shifted toward higher frequency compared to those of 40L30B30S and 40L50B10S, indicating the decoupling of vibrational and librational motions. These results suggest that coupling motion is correlated with low conductivity. The enhancement of conduction by the coupling of Li^+ vibration and libration was reported in polyanions for solid-state phosphosulfide and *closو*-borate electrolytes.^{59–61} This phenomenon was attributed to the “paddle-wheel effect” of polyanion rotation, which can effectively assist Li^+ translation from one polyanion to another. These materials have relatively high ionic conductivities (approximately 3 or 4 orders of magnitude higher than those of the oxide glasses in this study). Thus, the coupling motion in these solid-state phosphosulfide and *closو*-borate electrolytes differs from that of Li^+ and O^1 in 40L30B30S and 40L50B10S, which have lower conductivity. Therefore, we assigned the coupling motion to harmonic vibration without Li^+ translation. The stationary vibration of Li^+ is coupled with O^1 libration in 40L30B30S and 40L50B10S, whereas the vibration of Li is relatively decoupled in 60L25B15S, which has higher conductivity than 40L30B30S and 40L50B10S. Therefore, the decoupling of motion between

host atoms and Li is a key to changing the macroscopic conductivity. We believe that this concept is important for the design of new solid-state electrolytes.

CONCLUSIONS

We probed the structure and dynamics of Li^+ in lithium borosilicate glasses with different Li contents and $\text{SiO}_2/\text{B}_2\text{O}_3$ ratios using AIMD simulations. The glasses were simulated using the melt-and-quench method with a relatively slow quenching rate (8 K/ps). The results reveal the formation of the boron 3-ring super structures in the glass network that were usually not observed in CMD simulations. This method overcomes a key limitation of CMD simulation. We also demonstrated the preferential coordination of Li^+ to O^1 (or nonbridging oxygen), indicating the significance of the interaction between Li^+ and O^1 for lithium ion diffusion and transport.

The dynamics of Li^+ were investigated in terms of the Li^+ MSD, and the coordination numbers of Li^+ with O^1 for Li ions with different mobilities. These analyses indicated the homogeneous distribution of Li^+ around various O^1 species, which are bonded to different cations (Si, B^{III} , B^{IV} , and $\text{B}_{\text{ring}}^{\text{III,IV}}$). Overlap between Li^+ vibration and O^1 libration was found in 40L30B30S and 40L50B10S, suggesting that Li^+ is strongly coupled to the librational motion of O^1 . This behavior differs from that observed in solid-state electrolytes with high conductivity (e.g., phosphosulfide). The decoupling of Li^+ vibration and O^1 libration was enhanced in 60L25B15S compared to in the other two compositions, resulting in the highest conductivity in this study. Consequently, the coupled motion in 40L30B30S and 40L50B10S mainly consists of the stationary motion of Li^+ , and the decoupled motion

contributes to increasing the macroscopic conductivity. This concept provides a useful insight for controlling the macroscopic conductivity of borosilicate glasses.

■ ASSOCIATED CONTENT

■ Supporting Information

The Supporting Information is available free of charge at <https://pubs.acs.org/doi/10.1021/acs.jpcc.1c00309>.

Summary of FEMTECK; mean-square displacements of Si, B, and O at 1600 K; detailed comparison with classical molecular dynamics; comparison with fitting procedure of ^{11}B MAS NMR spectra; visualization of the boron 3-ring super structures; and pair correlation functions of Si–O, B–O, (O^I, O^{II}, and B^{IV})–Li (PDF)

■ AUTHOR INFORMATION

Corresponding Author

Takahiro Ohkubo – Graduate School of Engineering, Chiba University, Chiba 263-8522, Japan;  orcid.org/0000-0001-8187-1470; Phone: +81 (0)43 2903435; Email: ohkubo.takahiro@faculty.chiba-u.jp; Fax: +81 (0) 43 2903431

Authors

Shingo Urata – Innovative Technology Laboratories, AGC, Inc., Yokohama 230-0045, Kanagawa, Japan
Yutaka Imamura – Innovative Technology Laboratories, AGC, Inc., Yokohama 230-0045, Kanagawa, Japan
Taketoshi Taniguchi – Innovative Technology Laboratories, AGC, Inc., Yokohama 230-0045, Kanagawa, Japan
Nanae Ishioka – Material Development Group, Frit Paste Division, AGC Electronics Co., Ltd., Yokohama 230-0045, Kanagawa, Japan
Masamichi Tanida – General Manager, Frit Paste Division, AGC Electronics Co., Ltd., Yokohama 230-0045, Kanagawa, Japan
Eiji Tsuchida – National Institute of Advanced Industrial Science and Technology (AIST), Tsukuba, Ibaraki 305-8568, Japan
Lu Deng – Department of Materials Science and Engineering, University of North Texas, Denton, Texas 76203, United States
Jincheng Du – Department of Materials Science and Engineering, University of North Texas, Denton, Texas 76203, United States;  orcid.org/0000-0003-4805-7498

Complete contact information is available at:

<https://pubs.acs.org/doi/10.1021/acs.jpcc.1c00309>

Notes

The authors declare no competing financial interest.
All trajectories and velocities AIMD simulations can be also provided upon request.

■ ACKNOWLEDGMENTS

This work was supported by the Akira Yoshino Research Grant of The Chemical Society of Japan. We acknowledge the computational resources provided by the Research Institute for Information Technology, Kyushu University.

■ REFERENCES

- (1) Kaup, K.; Bazak, J. D.; Vajargah, S. H.; Wu, X.; Kulisch, J.; Goward, G. R.; Nazar, L. F. A Lithium Oxythioborosilicate Solid Electrolyte Glass with Superionic Conductivity. *Adv. Energy Mater.* **2020**, *10*, 1902783.
- (2) Martin, S. W.; Christensen, R.; Olson, G.; Kieffer, J.; Wang, W. New interpretation of Na⁺ -ion conduction in and the structures and properties of sodium borosilicate mixed glass former glasses. *J. Phys. Chem. C* **2019**, *123*, 5853–5870.
- (3) Muralidharan, P.; Venkateswarlu, M.; Satyanarayana, N. Sol–gel synthesis, structural and ion transport studies of lithium borosilicate glasses. *Solid State Ionics* **2004**, *166*, 27–38.
- (4) Maia, L. F.; Rodrigues, A. C. Electrical conductivity and relaxation frequency of lithium borosilicate glasses. *Solid State Ionics* **2004**, *168*, 87–92.
- (5) Kim, C. E.; Hwang, H. C.; Yoon, M. Y.; Choi, B. H.; Hwang, H. J. Fabrication of a high lithium ion conducting lithium borosilicate glass. *J. Non-Cryst. Solids* **2011**, *357*, 2863–2867.
- (6) Deshpande, V.; Raut, A. Effect of gamma irradiation on the density, glass transition temperature and electrical conductivity of lithium borosilicate glasses with alumina addition. *J. Non-Cryst. Solids* **2017**, *457*, 104–110.
- (7) Fan, H.; del Campo, L.; Montouillout, V.; Malki, M. Ionic conductivity and boron anomaly in binary lithium borate melts. *J. Non-Cryst. Solids* **2020**, *543*, 120160.
- (8) Montouillout, V.; Fan, H.; del Campo, L.; Ory, S.; Rakhmatullin, A.; Fayon, F.; Malki, M. Ionic conductivity of lithium borate glasses and local structure probed by high resolution solid-state NMR. *J. Non-Cryst. Solids* **2018**, *484*, 57–64.
- (9) Neyret, M.; Lenoir, M.; Grandjean, A.; Massoni, N.; Penelon, B.; Malki, M. Ionic transport of alkali in borosilicate glass. Role of alkali nature on glass structure and on ionic conductivity at the glassy state. *J. Non-Cryst. Solids* **2015**, *410*, 74–81.
- (10) Meikhall, M.; Gohar, I.; Megahed, A. Lithium borosilicate glasses as electrolyte for solid state batteries. *J. Phys. D: Appl. Phys.* **1993**, *26*, 1125.
- (11) Enke, D.; Janowski, F.; Schwieger, W. Porous glasses in the 21st century—a short review. *Microporous Mesoporous Mater.* **2003**, *60*, 19–30.
- (12) Charles, R. Phase separation in borosilicate glasses. *J. Am. Ceram. Soc.* **1964**, *47*, 559–563.
- (13) Yazawa, T.; Kuraoka, K.; Akai, T.; Umesaki, N.; Du, W.-F. Clarification of phase separation mechanism of sodium borosilicate glasses in early stage by nuclear magnetic resonance. *J. Phys. Chem. B* **2000**, *104*, 2109–2116.
- (14) Sander, S. A.; Weiss, M.; Denecke, R.; Enke, D.; Roggendorf, H. Long-Term Heat Treatment of Phase Separating Sodium Borosilicate Glass. *Adv. Eng. Mater.* **2019**, *21*, 1900187.
- (15) Cussen, E. J. The structure of lithium garnets: cation disorder and clustering in a new family of fast Li⁺ conductors. *Chem. Commun.* **2006**, 412–413.
- (16) Jalem, R.; Yamamoto, Y.; Shiiba, H.; Nakayama, M.; Munakata, H.; Kasuga, T.; Kanamura, K. Concerted migration mechanism in the Li ion dynamics of garnet-type Li₇La₃Zr₂O₁₂. *Chem. Mater.* **2013**, *25*, 425–430.
- (17) Mo, Y.; Ong, S. P.; Ceder, G. First principles study of the Li₁₀GeP₂S₁₂ lithium super ionic conductor material. *Chem. Mater.* **2012**, *24*, 15–17.
- (18) Guillot, B.; Sator, N. A computer simulation study of natural silicate melts. Part II: High pressure properties. *Geochim. Cosmochim. Acta* **2007**, *71*, 4538–4556.
- (19) Wang, M.; Anoop Krishnan, N. M.; Wang, B.; Smedskjaer, M. M.; Mauro, J. C.; Bauchy, M. A new transferable interatomic potential for molecular dynamics simulations of borosilicate glasses. *J. Non-Cryst. Solids* **2018**, *498*, 294–304.
- (20) Delaye, J.-M.; Ghaleb, D. Combining two types of molecular dynamics for rapid computation of high-energy displacement cascades. I. Description of the method. *Phys. Rev. B: Condens. Matter Mater. Phys.* **2005**, *71*, 224203.
- (21) Habasaki, J.; Okada, I. Molecular dynamics study of Li₂SiO₃ in the liquid and glassy states. *Mol. Simul.* **1992**, *8*, 179–195.

- (22) Prasada Rao, R.; Tho, T. D.; Adams, S. Ion transport pathways in molecular dynamics simulated lithium silicate glasses. *Solid State Ionics* **2010**, *181*, 1–6.
- (23) Habasaki, J.; Ngai, K.; Hiwatari, Y. Molecular dynamics study of cage decay, near constant loss, and crossover to cooperative ion hopping in lithium metasilicate. *Phys. Rev. E: Stat. Phys., Plasmas, Fluids, Relat. Interdiscip. Top.* **2002**, *66*, 021205.
- (24) Kunow, M.; Heuer, A. Nonlinear ionic conductivity of lithium silicate glass studied via molecular dynamics simulations. *J. Chem. Phys.* **2006**, *124*, 214703.
- (25) Li, W.; Garofalini, S. H. Molecular dynamics simulation of lithium diffusion in $\text{Li}_2\text{O}-\text{Al}_2\text{O}_3-\text{SiO}_2$ glasses. *Solid State Ionics* **2004**, *166*, 365–373.
- (26) Habasaki, J.; Hiwatari, Y. Characteristics of slow and fast ion dynamics in a lithium metasilicate glass. *Phys. Rev. E: Stat. Phys., Plasmas, Fluids, Relat. Interdiscip. Top.* **1999**, *59*, 6962.
- (27) Habasaki, J.; Ngai, K. Refinements in the characterization of the heterogeneous dynamics of Li ions in lithium metasilicate. *J. Chem. Phys.* **2008**, *129*, 034503.
- (28) Deng, L.; Du, J. Development of boron oxide potentials for computer simulations of multicomponent oxide glasses. *J. Am. Ceram. Soc.* **2018**, *102*, 2482–2505.
- (29) Wright, A. C. Borate structures: crystalline and vitreous. *Phys. Chem. Glasses: Eur. J. Glass Sci. Technol., Part B* **2010**, *51*, 1–39.
- (30) Maranas, J. K.; Chen, Y.; Stillinger, D. K.; Stillinger, F. H. Polarization interactions and boroxol ring formation in boron oxide: A molecular dynamics study. *J. Chem. Phys.* **2001**, *115*, 6578–6589.
- (31) Alderman, O. L.; Ferlat, G.; Baroni, A.; Salanne, M.; Micoulaut, M.; Benmore, C.; Lin, A.; Tamalonis, A.; Weber, J. Liquid B_2O_3 up to 1700 K: X-ray diffraction and boroxol ring dissolution. *J. Phys.: Condens. Matter* **2015**, *27*, 455104.
- (32) Inoue, H.; Masuno, A.; Watanabe, Y. Modeling of the structure of sodium borosilicate glasses using pair potentials. *J. Phys. Chem. B* **2012**, *116*, 12325–12331.
- (33) Stevenson, B.; Yu, Y.; Edén, M. Structure–composition trends in multicomponent borosilicate-based glasses deduced from molecular dynamics simulations with improved B–O and P–O force fields. *Phys. Chem. Chem. Phys.* **2018**, *20*, 8192–8209.
- (34) Yu, Y.; Stevenson, B.; Edén, M. Direct Experimental Evidence for Abundant BO_4-BO_4 Motifs in Borosilicate Glasses From Double-Quantum ^{11}B NMR Spectroscopy. *J. Phys. Chem. Lett.* **2018**, *9*, 6372–6376.
- (35) Pacaud, F.; Delaye, J.-M.; Charpentier, T.; Cormier, L.; Salanne, M. Structural study of $\text{Na}_2\text{O}-\text{B}_2\text{O}_3-\text{SiO}_2$ glasses from molecular simulations using a polarizable force field. *J. Chem. Phys.* **2017**, *147*, 161711.
- (36) Pedesseau, L.; Ispas, S.; Kob, W. First-principles study of a sodium borosilicate glass-former. II. The glass state. *Phys. Rev. B: Condens. Matter Mater. Phys.* **2015**, *91*, 134202.
- (37) Pedesseau, L.; Ispas, S.; Kob, W. First-principles study of a sodium borosilicate glass-former. I. The liquid state. *Phys. Rev. B: Condens. Matter Mater. Phys.* **2015**, *91*, 134201.
- (38) Ohkubo, T.; Tsuchida, E.; Deguchi, K.; Ohki, S.; Shimizu, T.; Otomo, T.; Iwadate, Y. Insights from ab initio molecular dynamics simulations for a multicomponent oxide glass. *J. Am. Ceram. Soc.* **2018**, *101*, 1122–1134.
- (39) Srivastava, D.; Venetos, M. C.; mrsimulator, P. J. v0.5.0: A fast solid-state NMR spectrum simulation/analysis library, Zenodo, 2020, DOI: [10.5281/zenodo.3978779](https://doi.org/10.5281/zenodo.3978779) (accessed December 1, 2020).
- (40) Tsuchida, E.; Tsukada, M. Large-Scale Electronic-Structure Calculations Based on the Adaptive Finite-Element Method. *J. Phys. Soc. Jpn.* **1998**, *67*, 3844–3858.
- (41) Tsuchida, E.; Tsukada, M. Adaptive Finite-Element Method for Electronic-Structure Calculations. *Phys. Rev. B: Condens. Matter Mater. Phys.* **1996**, *54*, 7602–7605.
- (42) Tsuchida, E.; Choe, Y.-K.; Ohkubo, T. An Adaptive Finite-Element Method for Large-Scale *Ab initio* Molecular Dynamics Simulations. *Phys. Chem. Chem. Phys.* **2015**, *17*, 31444–31452.
- (43) Goedecker, S.; Teter, M.; Hutter, J. Separable Dual-space Gaussian Pseudopotentials. *Phys. Rev. B: Condens. Matter Mater. Phys.* **1996**, *54*, 1703–1710.
- (44) Hartwigsen, C.; Goedecker, S.; Hutter, J. Relativistic separable dual-space Gaussian pseudopotentials from H to Rn. *Phys. Rev. B: Condens. Matter Mater. Phys.* **1998**, *58*, 3641.
- (45) Lu, X.; Deng, L.; Kuo, P.-H.; Ren, M.; Buterbaugh, I.; Du, J. Effects of boron oxide substitution on the structure and bioactivity of SrO -containing bioactive glasses. *J. Mater. Sci.* **2017**, *52*, 8793–8811.
- (46) Plimpton, S. Fast parallel algorithms for short-range molecular dynamics. *J. Comput. Phys.* **1995**, *117*, 1–19.
- (47) Fortino, M.; Berselli, A.; Stone-Weiss, N.; Deng, L.; Goel, A.; Du, J.; Pedone, A. Assessment of interatomic parameters for the reproduction of borosilicate glass structures via DFT-GIPAW calculations. *J. Am. Ceram. Soc.* **2019**, *102*, 7225–7243.
- (48) Koller, H.; Engelhardt, G.; Kentgens, A. P.; Sauer, J. ^{23}Na NMR spectroscopy of solids: interpretation of quadrupole interaction parameters and chemical shifts. *J. Phys. Chem.* **1994**, *98*, 1544–1551.
- (49) Du, L.-S.; Stebbins, J. F. Solid-state NMR study of metastable immiscibility in alkali borosilicate glasses. *J. Non-Cryst. Solids* **2003**, *315*, 239–255.
- (50) Du, L.-S.; Stebbins, J. F. Nature of silicon–boron mixing in sodium borosilicate glasses: a high-resolution ^{11}B and ^{17}O NMR study. *J. Phys. Chem. B* **2003**, *107*, 10063–10076.
- (51) Du, L.-S.; Stebbins, J. F. Network connectivity in aluminoborosilicate glasses: A high-resolution ^{11}B , ^{27}Al and ^{17}O NMR study. *J. Non-Cryst. Solids* **2005**, *351*, 3508–3520.
- (52) Dell, W.; Bray, P.; Xiao, S. ^{11}B NMR studies and structural modeling of $\text{Na}_2\text{O}-\text{B}_2\text{O}_3-\text{SiO}_2$ glasses of high soda content. *J. Non-Cryst. Solids* **1983**, *58*, 1–16.
- (53) Zhong, J.; Wu, X.; Liu, M.; Bray, P. Structural modeling of lithium borosilicate glasses via NMR studies. *J. Non-Cryst. Solids* **1988**, *107*, 81–87.
- (54) Ganster, P.; Benoit, M.; Kob, W.; Delaye, J.-M. Structural properties of a calcium aluminosilicate glass from molecular-dynamics simulations: A finite size effects study. *J. Chem. Phys.* **2004**, *120*, 10172–10181.
- (55) Alderman, O.; Liska, M.; Machacek, J.; Benmore, C.; Lin, A.; Tamalonis, A.; Weber, J. Temperature-driven structural transitions in molten sodium borates $\text{Na}_2\text{O}-\text{B}_2\text{O}_3$: X-ray diffraction, thermodynamic modeling, and implications for topological constraint theory. *J. Phys. Chem. C* **2016**, *120*, 553–560.
- (56) Masayoshi Ihara, M. Y.; Krogh-Moe, J. Crystal structure of lithium triborate, $\text{Li}_2\text{O}(\text{B}_2\text{O}_3)_3$. *J. Ceram. Soc. Jpn.* **1980**, *88*, 179–184.
- (57) Secco, E. Paddle wheel mechanism in lithium sulfates: Arguments in defense and evidence against. *J. Solid State Chem.* **1992**, *96*, 366–375.
- (58) Hansen, J.-P.; McDonald, I. R. *Theory of Simple Liquids*; Harcourt Brace Jovanovich, New York, 1990.
- (59) Kweon, K. E.; Varley, J. B.; Shea, P.; Adelstein, N.; Mehta, P.; Heo, T. W.; Udoovic, T. J.; Stavila, V.; Wood, B. C. Structural, chemical, and dynamical frustration: origins of superionic conductivity in closo-borate solid electrolytes. *Chem. Mater.* **2017**, *29*, 9142–9153.
- (60) Smith, J. G.; Siegel, D. J. Low-temperature paddlewheel effect in glassy solid electrolytes. *Nat. Commun.* **2020**, *11*, 1483.
- (61) Ohkubo, T.; Ohara, K.; Tsuchida, E. Conduction mechanism in 70 Li₂S-30 P₂S₅ glass by ab initio molecular dynamics simulations: Comparison with Li₇P₃S₁₁ crystal. *ACS Appl. Mater. Interfaces* **2020**, *12*, 25736–25747.